A&A, 707, A350 (2026)
https://doi.org/10.1051/0004-6361/202558729

Astronomy & Astrophysics

A deep MeerKAT view of associated H I absorption in radio AGNs at intermediate redshift: Role of absorber geometry and conditions of the gas

Raffaella Morganti[1,2,⋆], Tom Oosterloo[1,2], Clive Tadhunter[3], and Suma Murthy[4,5]

[1] ASTRON, The Netherlands Institute for Radio Astronomy, Oude Hoogeveensedijk 4, 7991 PD Dwingeloo, The Netherlands
[2] Kapteyn Astronomical Institute, University of Groningen, Postbus 800, 9700 AV Groningen, The Netherlands
[3] Department of Physics and Astronomy, University of Sheffield, Sheffield S7 3RH, UK
[4] Joint ALMA Observatory, Alonso de Córdova 3107, Vitacura, Casilla 19001, Santiago de Chile, Chile
[5] Joint Institute for VLBI ERIC, Oude Hoogeveensedijk 4, 7991 PD Dwingeloo, The Netherlands

Received 22 December 2025 / Accepted 1 February 2026

ABSTRACT

We present MeerKAT observations searching for H I absorption in a sample of 17 powerful ($L_{1.4\,\mathrm{GHz}} > 10^{27}\,\mathrm{W\,Hz^{-1}}$) radio sources at intermediate redshifts ($0.25 < z < 0.7$). The sample is well characterised at radio and optical wavelengths, allowing us to connect the presence (or absence) of H I to the properties of the active galactic nucleus (AGN) and its host galaxy. The sample consists mostly of core-dominated sources and quasars. Half of the targets have a UV luminosity below the limit of $L_{\mathrm{UV}} = 10^{23}\,\mathrm{W\,Hz^{-1}}$, whereby at values above this limit, the gas would be expected to be ionised by this radiation. We obtained 15 spectra free (or almost free) of radio frequency interference, reaching extremely low optical depths ($\tau_{\mathrm{peak}} < 0.005$) resulting in three new H I absorption detections. Two are associated H I absorptions, giving a detection rate of such systems of 13%±7%. Both are found in a young radio source (PKS 1151–34 and PKS 1306–09), confirming the trend that this type of sources are more often detected in H I compared to more evolved ones. The UV luminosity of both these sources is below $10^{23}\,\mathrm{W\,Hz^{-1}}$. Surprisingly, one of the detections (PKS 1151–34) is hosted by a quasar, suggesting that the radio lobes of this source are still embedded in the circumnuclear disc. In the second source (PKS 1306–09), the H I is highly blueshifted and likely part of the jet-driven outflow earlier observed in the warm ionised gas. This represents a new addition to the group of young radio AGNs, where multi-phased outflows have been observed as predicted by numerical simulations. A third detection is a 'local intervening' system, caused by a galaxy in the local environment of PKS 0405–12 and located in front of the southern radio lobe of this source, about 100 kpc in projection from this quasar. More such cases are expected to show up in large, blind surveys and our results show the need for high spatial resolution and good ancillary data to separate associated from intervening absorption. Overall, the results indicate a variety of plausible situations, which resemble what is seen at low redshifts. For the associated absorption, a combination of evolutionary status of the radio sources, physical conditions, and geometry of the gas structure determine the detection rate of H I absorption. The data also show the excellent capabilities of MeerKAT for obtaining very low optical depth detections, revealing the presence of an otherwise missed group of absorptions.

Key words. ISM: jets and outflows – galaxies: active – galaxies: ISM – galaxies: jets

1. Introduction

The presence and properties of the cold gas ($T \ll 10^4\,\mathrm{K}$) in galaxies play a crucial role in tracing their evolution and star formation history (e.g. Saintonge & Catinella 2022; Crain & van de Voort 2023). Furthermore, this gas can be relevant for providing the fuel for turning a dormant super-massive black hole (SMBH) into an active galactic nucleus (AGN), as well as for tracing the effects of the energy released by the AGN. Thus, there are several reasons for studying the cold gas in galaxies hosting an AGN. Although the various phases of this gas (atomic neutral and molecular) are usually detected in emission, absorption observations can provide a complementary way of tracing this gas (e.g. Morganti 2024; Rose et al. 2024).

H I 21-cm absorption observations have been used for many years to trace both intervening gas (i.e. gas unrelated to the AGN host and observed along the line of sight; Kanekar & Briggs 2004), as well as gas associated with the AGN host (see Morganti & Oosterloo 2018; Morganti 2024 for overviews). Although they differ in nature, they are both important for tracing the evolution of the presence and properties of H I in and between galaxies.

Here, we focus on associated H I absorption which traces atomic hydrogen located mainly in the central circumnuclear regions of radio AGNs. The interpretation of absorption observations is complicated by the fact that only gas in front of the radio continuum can be traced. In addition, due to the dependence of the optical depth on the spin temperature, there is a bias towards detecting the colder H I. However, these observations do offer other advantages that can be exploited. In particular, using VLBI observations, absorption observations can trace H I gas down to pc scales and – as long as the background continuum is strong enough – it can be used to trace the H I in objects with redshifts much higher than can typically be done using H I in emission. Here, we focus on H I absorption observations of a sample of radio sources at intermediate redshifts ($0.26 < z < 0.67$).

According to Aditya et al. (2024), about a thousand radio sources (mostly radio AGNs) have been observed to investigate their associated H I absorption, with the vast majority of the detections being made at low redshift (i.e. $z < 0.2$ or, equivalently, at $\nu > 1200$ MHz), where the detection rate ranges between 10 and 40% (see below). The redshift limit of $z = 0.2$

⋆ Corresponding author: morganti@astron.nl

is mostly set by the limited capabilities of the receivers available in radio telescopes to observe at lower frequencies. However, the situation has changed in recent years, thanks to radio telescopes such as the uGMRT, MeerKAT, and ASKAP, thanks to their capacity to conduct observations at frequencies well below 1200 MHz. For the study of H I in radio AGNs, observations using radio interferometers are more suitable than those done with single-dish telescopes because of their higher angular resolution and bandpass stability; the relevance of this will become clear in the present study.

For low-redshift sources, as we now know thanks to recent absorption studies, H I can be associated with all the key circumnuclear structures of AGNs (see e.g. Morganti & Oosterloo 2018 for a review). The most prevalent H I structures are discs and rings. The gas in these is not always kinematically relaxed, but can have high velocity dispersion and/or is undergoing fast outflows (see Morganti et al. 2003 and Murthy et al. 2024 and refs therein for examples). In addition, clouds of infalling gas are seen in some objects (van Gorkom et al. 1989; Tremblay et al. 2016; Maccagni et al. 2018, 2023 and refs therein), possibly related to feeding the SMBH. More rarely, clouds of quiescent gas at larger distances from the centre, albeit still bound to the host galaxy, are observed (e.g. Morganti et al. 2009; Struve & Conway 2012).

The detection of H I in absorption is also connected to the type of radio AGNs observed and this reflects on their detection rate. For example, the group of young (or recently restarted) radio sources (with ages $<10^6$ yr), which are identified by being compact and having a peaked or steep radio spectrum (i.e. CSS and GPS, O'Dea & Saikia 2021), have the highest detection rate at both low and high redshift (see below for more details). This is likely due to the combination of two factors. The first is the (sub-)kpc size of the radio continuum of these sources, which roughly matches the scale of the gas discs and rings. The second is the fact that these young sources are typically in a gas-rich phase which also provides the fuel for the radio AGN. Detection rates up to 40% have been found for such sources (e.g. Vermeulen et al. 2003; Gupta et al. 2006; Chandola et al. 2011; Geréb et al. 2015; Glowacki et al. 2017) and the H I often shows disturbed kinematics (e.g. Struve & Conway 2012; Schulz et al. 2018, 2021; Murthy et al. 2024), suggesting an interaction between the jets and the ISM, as also predicted by the simulations (Mukherjee et al. 2018; Perucho 2024; Dutta et al. 2024).

Extended radio sources show a lower detection rate (roughly 10%; Morganti et al. 2001; Chandola et al. 2013), but with large scatter due to the low number of objects observed. However, broad-line galaxies and BL Lac objects are typically not detected. This suggests the H I is mostly associated with nuclear tori and discs which would be, as predicted by unified schemes of AGNs (Tadhunter 2008), seen face-on in broad-line objects and not, thus, in front of the radio continuum.

Unsurprisingly, the detection rate of H I in absorption is lower than found for H I emission (about 40%; Serra 2012) for early-type galaxies (the typical hosts of radio AGNs); nevertheless, the results above show that H I absorption can help trace the presence of H I. In this respect, it is also interesting to explore higher redshift objects that emission studies cannot reach easily.

2. Associated H I absorption at higher redshift ($z > 0.2$)

Studies of associated H I absorption at higher redshift tend to show a more complex view of the presence and properties of this

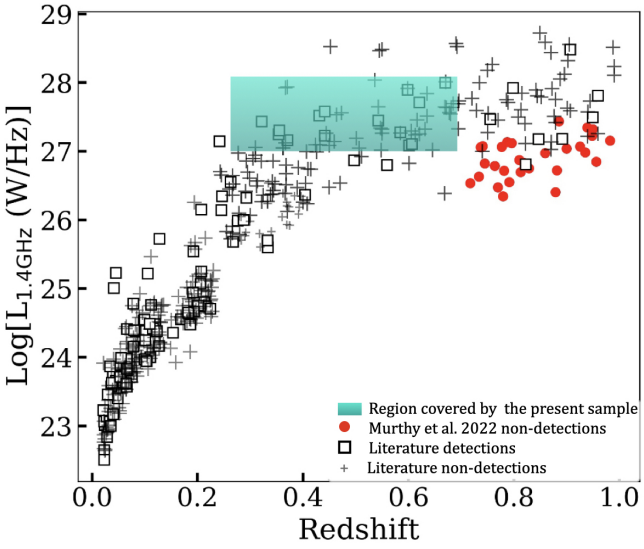

Fig. 1. Distribution of the radio luminosities for sources in various samples available in literature, adapted from Murthy et al. (2022). Location of the present sample is indicated as the green area.

gas, although the number of observations is still relatively small (see the reviews of Dutta et al. 2022 and Morganti 2024). In general, there is a tendency to find a lower detection rate ($\ll 10\%$) of H I absorption at $z > 0.2$, which becomes even more pronounced for $z > 1$ (Curran et al. 2008). There is no agreement on what is the cause of this trend. The physical conditions of the gas can be influenced by high levels of UV radiation, which can be expected to be present in the powerful sources typically observed at high z. Curran et al. (2008) proposed a limit to the UV luminosity of $L_{\rm UV} = 10^{23}\,{\rm W\,Hz^{-1}}$ above which the H I would be ionised, thereby reducing the detection rate (Curran et al. 2008, 2013; Aditya et al. 2016; Curran et al. 2017; Aditya & Kanekar 2018a). However, that other factors may also be relevant is suggested by the fact that H I absorption has been detected in some objects with a UV luminosity higher than the $10^{23}\,{\rm W\,Hz^{-1}}$ limit (e.g. Aditya et al. 2017, 2021) and by the low detection rate even for samples of sources selected with $L_{\rm UV} < 10^{23}\,{\rm W\,Hz^{-1}}$ (Murthy et al. 2022).

As an alternative, the detection rate may depend on the properties and the types of sources observed. As can be seen from Fig. 1, most of the AGNs observed in H I absorption at redshift $z > 0.2$ (referred to as high-z AGNs in this work) are different from those observed at low z; they typically have higher radio power ($L_{1.4\ {\rm GHz}} > 10^{26}\,{\rm W\,Hz^{-1}}$) than the low-$z$ sources which mostly lie below this limit (see Fig. 1). In addition, the high-z samples have a higher fraction of quasars and flat-spectrum objects (i.e. most targets have been selected from flat spectrum samples). In such cases, the detection of a circumnuclear disc of H I can be hampered by orientation effects as is seen at low z (e.g. Murthy et al. 2021) . The presence of a strong radio AGNs can also affect the detectability by the increase in the $T_{\rm spin}$ of the gas in the nuclear regions due to the strong radio flux (Bahcall & Ekers 1969) and the consequent decrease in the optical depth for a given column density.

Interestingly, several high-z studies find that compact, peaked spectrum sources tend to maintain their higher detection rate at high redshifts (see e.g. Aditya & Kanekar 2018b), although this finding is still based on limited statistics. This appears to be further confirmed by the initial results of blind

Table 1. Observational parameters.

Source		z	ν_{obs} (GHz)	Δv (km s^{-1})	Beam ($''\times''$)	PA ($^\circ$)	σ_{cont} (mJy beam^{-1})	σ_{line} (mJy beam^{-1})	Notes/Refs
PKS 0159–11	Q	0.669	851.05	11.7	9.3×8.6	0.9	0.08	0.64	1,5
PKS 0252–71	G	0.56443 ± 0.00003^a	907.02	11.0	13.3×6.3	144.1	0.14	1.74	2,3,5
PKS 0403–13	Q	0.571	904.14	11.0	8.9×7.6	166.3	0.30	0.85	4,5
PKS 0405–12	Q	0.574	902.41	11.0	9.3×8.3	40.2	0.37	0.68	5,4
PKS 0637–75	Q	0.651	860.33	11.0	17.4×6.2	103.9	0.11	1.07	6
PKS 0842–75	Q	0.524	932.02	–	–	–	–	–	6 (RFI)
PKS 0859–25	G	0.305	1088.43	–	7.8×6.0	171.1	0.17	–	5 (RFI)
PKS 1136–13	Q	0.544	914.03	10.9	9.6×7.2	150.9	0.35	0.91	5,7
PKS 1151–34	Q	0.2579 ± 0.0001^a	1129.09	6.9	9.5×5.8	141.2	0.57	1.86	2,3,5
PKS 1306–09	G	0.46692 ± 0.00007^a	970.22	10.2	12.2×6.9	159.7	0.60	1.14	2,3,5
PKS 1355–41	Q	0.313	1081.80	14.5	9.8×6.2	132.2	0.08	0.66	6
PKS 1510–08	Q	0.361	1043.64	7.5	10.5×6.7	131.3	0.09	0.69	5,8
PKS 1602+01	BLG	0.462	971.55	10.2	11.5×8.3	116.4	0.10	0.97	5,9,10
PKS 1954–388	Q	0.63	871.41	11.4	10.2×7.1	20.4	0.05	0.55	5
PKS 2203–18	Q	0.618	877.87	11.3	9.2×7.5	170.2	0.24	1.19	5
PKS 2243–123	Q	0.63	871.41	11.4	9.1×8.3	176.4	0.07	0.59	4,5,11
PKS 2345–16	Q	0.576	901.27	11.0	10.1×8.1	48.1	0.14	0.77	4,5

Notes. The redshifts of most of the observed galaxies are taken from Tadhunter et al. (1993). [(a)]Redshifts are taken from Santoro et al. (2020) and are based on the measurement of the stellar absorption lines associated with the host galaxy starlight. Note that Santoro et al. (2020) did not correct the redshifts to heliocentric. For PKS 1151–34 this correction for the redshift is +0.000083, while for PKS 1306–09 it is +0.000096. The beam sizes are those of the continuum images. References: (1) Reid et al. (1999); (2) Tzioumis et al. (2002); (3) Santoro et al. (2020); (4) Cheng et al. (2020); (5) Morganti et al. (1993); (6) Burgess & Hunstead (2006); (7) Fernini (2014); (8) Lister et al. (2009); (9) Morganti et al. (1999); (10) Tadhunter et al. (2002); (11) Cheng et al. (2023)

surveys such as FLASH (Yoon et al. 2025). Thus, the conditions of the gas in the very centre can can make it possible to detect the presence of atomic hydrogen even at high z.

In summary, H I absorption studies at $z > 0.2$ are giving mixed results about whether H I is indeed present less frequently at $z > 0.2$ in radio AGNs (unlike what is seen in molecular gas; Audibert et al. 2022). Understanding the role of selection effects not only requires larger samples, but also a better characterisation of the targets. While the blind surveys that are now becoming available (e.g. FLASH; Yoon et al. 2025) can give a view of the presence of H I in a larger number of objects, there is still a need to investigate possible trends and biases and connect the detection rates and properties of the absorption. To do so, for example, we can use the strength and morphology of the background continuum, the types of radio and optical AGNs, and other factors.

Here, we present the search for H I absorption in a sample of powerful radio sources (see Fig. 1) extracted from the 2-Jy sample, which has been well studied in several wavebands (see description below). We have taken advantage of the capabilities and the location of MeerKAT telescope to observe sources in the redshift range $0.2 < z < 0.7$. For the strong sources in the sample, we have been able to reach very low optical depths of the H I 21-cm absorption thanks to the stability of the MeerKAT receiver system.

The paper is organised as follows. In Sect. 3, we describe the selection of the targets with a brief recap of the 2-Jy sample. In Sect. 4, we describe the new MeerKAT observations and the data reduction. In Sect. 5, we describe the general findings as well as the properties of the detected targets. We discuss the possible implications of our findings in Sect. 6. All distances, spatial scales, and luminosities were calculated assuming a flat Universe with $\Omega_M = 0.286$, $\Omega_{vac} = 0.714$, and $H_\circ = 69.6$ km s^{-1} Mpc^{-1}.

The target sources represent a complete sub-set of the so-called 2-Jy sample including southern ($\delta < +10^\circ$) radio sources with high 2.7-GHz radio fluxes ($S_{2.7\,GHz} > 2$ Jy; see Tadhunter 2016 for an overview of the 2-Jy sample). Here, we focus on sources with redshift $0.25 < z < 0.7$ and the targets and their redshifts are listed in Table 1. The sample has been well characterised in multiple bands, especially at radio (VLA/ATCA/VLBI; Morganti et al. (1993, 2001), Tzioumis et al. (2002), Morganti et al. (1999)) and optical wavelengths (NTT/VLT/Gemini; Tadhunter et al. 1993, 1998; Holt et al. 2008; Ramos Almeida et al. 2011). Because of the redshift limit ($z < 0.7$), the presence of optical emission lines, including Hα+[N II], could be observed for the sources in the sample to fully characterise the spectral properties. Part of the sample has also been observed with ALMA to investigate the properties of the molecular gas (in particular, focussing on CO(1–0); Tadhunter et al. 2024), while the study of the cold ISM traced by Herschel is reported in Bernhard et al. (2022) and Dicken et al. (2023). However, some of these studies have excluded the flat spectrum sources which dominate the present sample (see below).

Because of a limited allocation of observing time (and on request of the MeerKAT time allocation committee), we have restricted the observed sample to sources with flux larger than 30 mJy (at 1.4 GHz) of the core or the central component. This resulted in 17 sources with $0.25 < z < 0.7$, with a strong preference for core dominated objects; of these sources, only 4 are radio galaxies, of which 1 is classified as a broad-line galaxy (Tadhunter et al. 2002). The rest are quasars (i.e. with broad permitted emission lines seen in the optical spectrum; see notes in Tadhunter et al. 1993). In radio, a number of them are variable and have been monitored at high spatial resolution and up to high energies (including γ-rays). In Table 1, we list some of the references to available radio observations.

Table 2. Parameters of the sources observed with MeerKAT.

Source	S_{tot} (Jy)	$\log L_{tot}$ (W Hz^{-1})	S_{core} (Jy)	ΔS_{peak} (mJy)	τ_{peak} (10^{-3})	$\int S\,dv$ (mJy km s^{-1})	W_{50} (km s^{-1})	W_{20} (km s^{-1})	W_0 (km s^{-1})	N_{HI} (10^{20} cm^{-2})	Morph	L_{UV} 1216 Å (10^{23} W Hz^{-1})
0159–11	3.615	28.05	3.280		<0.59					<0.07	E	120
0252–71	8.879	28.24	8.879		<0.59					<0.07	U	0.02
0403–13	4.964	28.00	4.964		<0.51					<0.09	U	1.9
0405–12	4.132	27.93	0.839[a]	4.5 ± 1.0[b]	4.76	372 ± 29	90 ± 20	125 ± 30	160 ± 20	0.81	E	22
0637–75	6.938	28.30	4.980		<0.64					<0.12	E	9.5
0842–75	–	–	–		–					–	E	17
0859–25	7.539	27.45	–		–					–	E	0.07
1136–13	6.332	28.00	2.280		<1.20					<0.22	E	3.8
1151–34	7.498	27.27	7.498	28.0 ± 2.0	4.0	5386 ± 105	157 ± 20	350 ± 25	450 ± 30	1.31	U	0.18
1306–09	5.429	27.79	5.429	4.5 ± 1.0	0.9	1072 ± 69	260 ± 30	405 ± 30	455 ± 30	0.36	U	0.08
1355–41	5.905	27.38	0.115		<17.1					<3.11	E	4.2
1510–08	3.332	27.29	1.470		<1.41					<0.26	E	0.60
1602+01	6.418	27.86	3.220		<0.90					<0.16	E	0.81
1954–388	1.195	27.50	0.947		<1.74					<0.32	E	1.20
2203–18	7.288	28.26	7.288		<0.49					<0.09	U	0.04
2243–123	1.692	27.65	1.580		<1.12					<0.20	E	2.10
2345–16	2.602	27.73	2.602		<0.89					<0.16	U	0.71

Notes. The continuum fluxes are obtained at the frequency of the H I observations; therefore, at 1.4 GHz in the rest frame at the redshift of the source and it is the same for the total luminosities. The column densities are assuming T_{spin} = 100 K and a covering factor c_f = 1. The upper limits to the column density are estimated using the 3-σ noise and a FWHM of the line of 100 km s^{-1}. [(a)]Flux of the peak of the southern lobe. [(b)]Absorption against the southern lobe.

Four of the targets are classified as CSS and, with the exception of PKS 1306–09, a peak in the radio SED at low frequency is also observed (Tzioumis et al. 2002; Callingham et al. 2017). Three of them (PKS 0252–71, PKS 1151–34 and PKS 1306–09) have been observed in radio with Very Long Baseline Interferometry by Tzioumis et al. (2002) and were studied in detail in the optical using X-shooter by Santoro et al. (2020). Radio observations of a fourth candidate (quasar PKS 2243–123) are presented in Cheng et al. (2023). As mentioned in the introduction, CSS sources are considered to be young radio sources where a newly born jet is in the process of expanding in the central kpc regions (O'Dea & Saikia 2021).

3. The targets

The restrictions on the selection of the objects that we could observe in the allocated time meant that classical FR II galaxies were ultimately excluded because their cores are typically weak. One exception is PKS 0859–25 due to the fact that, unfortunately, the data were overly affected by radio frequency interference (RFI). Thus, this selection has introduced a bias in the observed sample which will be considered in the discussion of the results. The types of sources in the present sample are very different from those studied in Morganti et al. (2001) for the low-z ($z < 0.2$) part of the 2-Jy sample. That sample included only four broad-line objects (and one BL Lac) and instead had a number of weak emission-line galaxies. This already illustrates some of the differences that are present when moving to relatively high-z radio sources. The targets of the present study are also strong radio sources as shown in the plot of the radio luminosity versus redshift of Fig. 1, modified from Murthy et al. (2022), where the comparison of the distribution of radio luminosities with those of other studies can be found.

For the discussion of the sample, it can also be useful to have the UV luminosities of the sources, considering the role expected it may play according to some studies (see Sect. 1). Curran et al. (2008) derived the UV luminosities at 1216 Å by extrapolation or interpolation of mostly the optical B and R band fluxes and subsequent studies have followed this approach. In the case of our sample, some objects have been observed by GALEX, while for the rest we extrapolated to 1216 Å from the shortest wavelength UV/optical wavelength for which we could find a flux measurement in the literature. We list the UV luminosities in Table 2 and we describe how they were derived in Appendix A.

4. MeerKAT observations and data reduction

The observations were carried out with MeerKAT in October and November 2022 under project SCI-20220822-RM-01. Although the redshifts of the sources were such that their H I line would not fall in a priori known RFI regions, the data of four objects were affected by RFI. In two cases (PKS 0842–75 and PKS 0859–25), the spectra turned out to be not usable, while in one case (PKS 1136–13), the RFI was intermittent and the data could be used after flagging. In one final case (PKS 1151–34), the RFI only affects part of the spectrum and avoids the range of redshifted H I. Thus, the final usable sample comprises 15 sources.

The sample sources were observed in five blocks, four in the UHF band and one with the L-band receiver, depending on the redshift of the sources. The observations were done with 62 antennas, and each target was observed for 1 h on-source. The UHF data cover the range 544–1088 MHz, while the L band covers the range 856–1712 MHz. The 32K mode of the SKA Reconfigurable Application Board (SKARAB) correlator has been used. We used either PKS 1934–63 or J0408–6545 as primary calibrator for the flux density scale, delay, and bandpass calibration. Given the fact that our targets are quite strong sources, each observation of a primary calibrator was 30 minutes in length; in addition, in each observation block of 5 h, a bandpass calibrator was observed at the start and at the end of the block in order to monitor variations in the bandpass calibration (see Appendix B for an example). The frequency of the redshifted H I for each source is listed in Table 1, together with the

observational details and the parameters of the final data products.

In each observing block of 5 h, several sources were observed using the full UHF- or L bandwidth. However, to reduce the data volume for the analysis, for each source a band of about 20 MHz was extracted, centred on the frequency of the redshifted H I. This small band was also used for obtaining the continuum images (see below). The full band can be used to do a blind exploration of the presence of H I in other radio sources in the field, which we will present in a future paper.

All calibration steps were done using the CASA software (McMullin et al. 2007), except for cleaning the images, which was done using WSClean (Offringa et al. 2014), and for subtracting the clean components from the visibilities, which was done using DP3 (Dijkema et al. 2023). The first step in the calibration was to determine the delay calibration using one of the primary calibrators. Next, a initial bandpass and flux calibration was done for the primary calibrators using a point source model. Using this initial calibration, images were made of the primary calibrators, which were self-calibrated in a standard way. The source model resulting from this was used as model in a second iteration for deriving an new flux and bandpass calibration, now taking other sources in the field into account as well. This second step gives an improvement of the bandpass calibration, which is needed because of the strong fluxes of our target sources.

For each target source, the calibration of the primary calibrator observed closest in time was used to cross calibrate the target observation. Given the high fluxes of the targets, no secondary calibrators were used in the calibration. Each target observation was self-calibrated iteratively using three iterations of phase calibration, followed by one iteration of amplitude calibration. Only direction-independent calibration was performed. The continuum images obtained in this way (using robust = – 1.5) have a typical resolution of 10 arcsec, a noise level varying between 0.07 and 0.6 mJy beam^{-1} and a typical dynamic range of a few times 10^4. The exception is PKS 0842–75, for which (due to RFI) a continuum image could not be generated (see Table 1). Figure 2 shows an example of a continuum image obtained in this study, where the high quality is clearly seen.

Given the large field of view of MeerKAT, in particular in the UHF band, the continuum subtraction has to be done by subtracting the sky model from the target visibilities. After this was done, a data cube was made using robust = 0 and with a velocity resolution of about 10 km s^{-1} (varying with redshift; see Table 1) covering a small area centred on the target source. Although the calibration and the sky model obtained are of high quality, some minor continuum residuals are still present in these data cubes, typically at the level of a few times the noise level. These residuals were subtracted from the data cubes using a Savitzky–Golay filter on the spectra. The noise level of the final data cubes is typically 1 mJy beam^{-1}.

As mentioned above, for one source (PKS 0842–75) the continuum image could not be made due to strong RFI affecting the band. Ten sources show extended radio continuum (listed in column 12 of Table 2), with cases of double-lobed structure and other sources where only a small extension is seen. In the vast majority of the sources, a prominent core is observed (as expected). The continuum images of the extended sources are shown in Appendix D.

5. Results

The results from our search for H I absorption are summarised in Table 2. Of the 15 sources for which the effects of RFI were negligible or limited, we detected H I absorption in three objects. Two are associated H I detections (PKS 1151–34 and PKS 1306–09). These two detections result in a detection rate of 13% ± 7% for the associated absorption. We defined the third detection (PKS 0405–12) as 'local intervening' because it is attributed to a foreground galaxy in the local environment of PKS 0405–12. The de-redshifted H I spectra of the detections are shown in Figs. 4, 5, and 6.

Interestingly, the two associated H I absorptions were found against CSS and peaked (i.e. young) radio sources, despite the fact that one of them (PKS 1151–34) is classified as quasar (see Sect. 5.1.1). These detections confirm the trend, which was already found at both low and high redshift, that young radio sources are more likely to be detected in H I (see also Sect. 6). The other two CSS and peaked sources in the sample were not detected.

The peak optical depth (given in column 6 of Table 2) is defined as $\tau_{\rm peak} = -\ln[1 - \Delta S/(S_{\rm cont} \times c_{\rm f})]$, where ΔS is the absorbed flux, $S_{\rm cont}$ the continuum flux (either total or core depending whether the source is unresolved or extended), and $c_{\rm f}$ is the covering factor, assumed to be unity. In cases of non-detection, the upper limit to the peak optical depth has been calculated using $3 \times \sigma_{\rm line}$. In the case of the local intervening detection in PKS 0405–12, the continuum flux used to derive $\tau_{\rm peak}$ is the one measured at the location of the absorption.

Looking at the values listed in Table 2, we can see, due to the combination of the strength of the radio continuum of the sources (and their cores) and the high sensitivity of the observations, the limits of $\tau_{\rm peak}$ are quite low, in many cases, $\tau_{\rm peak}$ is even smaller that 0.001 (0.1%). Also the two detections of associated absorption have low optical optical depths between 0.004 and 0.0009 (0.4% and 0.09%). This is illustrated in Fig. 3 where the $\tau_{\rm peak}$ of the objects in our sample are compared with literature findings taken from Maccagni et al. (2017), which is representative of the variety among low-z radio sources. Although some cases of such low optical depth are also seen at low-z, the detections in our sample have $\tau_{\rm peak}$ values that are well below the peak of the distribution of the low-z detections. In Maccagni et al. (2017), only 3 out of 248 objects have $\tau_{\rm peak} \lesssim 0.005$. Interestingly, two of these are young radio sources. Also our upper limits cover a very different range compared than the distributions shown in Fig. 3.

For the detections, Table 2 lists, in addition to $\tau_{\rm peak}$ values, the width of the absorption lines and the column densities. The values of the column densities presented in Table 2 are normalised for $T_{\rm spin}$ and covering factor. The integrated column density has been estimated as $N_{\rm H\,I} = 1.83 \times 10^{18} T_{\rm spin}/c_{\rm f} \int \tau dv$. For the non-detections, a width of 100 km s^{-1} has been assumed. For the usually assumed values of $T_{\rm spin} = 100$ K and $c_{\rm f} = 1$, the upper limits to the column densities are relatively low, below 10^{20} cm^{-2}. We discuss these assumptions, in particular $T_{\rm spin}$ for PKS 1151–34, below.

5.1. Young radio sources detected in H I

The associated H I detections are found in two of the young (CSS) radio sources: PKS 1151–34 and PKS 1306–09. A discussion of their radio properties is provided in Tzioumis et al. (2002). Their H I profiles are shown in Figs 4 and 5. In both sources, the warm ionised gas has been studied in detail, recently using X-shooter by Santoro et al. (2020). As often seen in young radio sources, both show kinematically disturbed ionised gas associated with outflows. The most extreme and extended

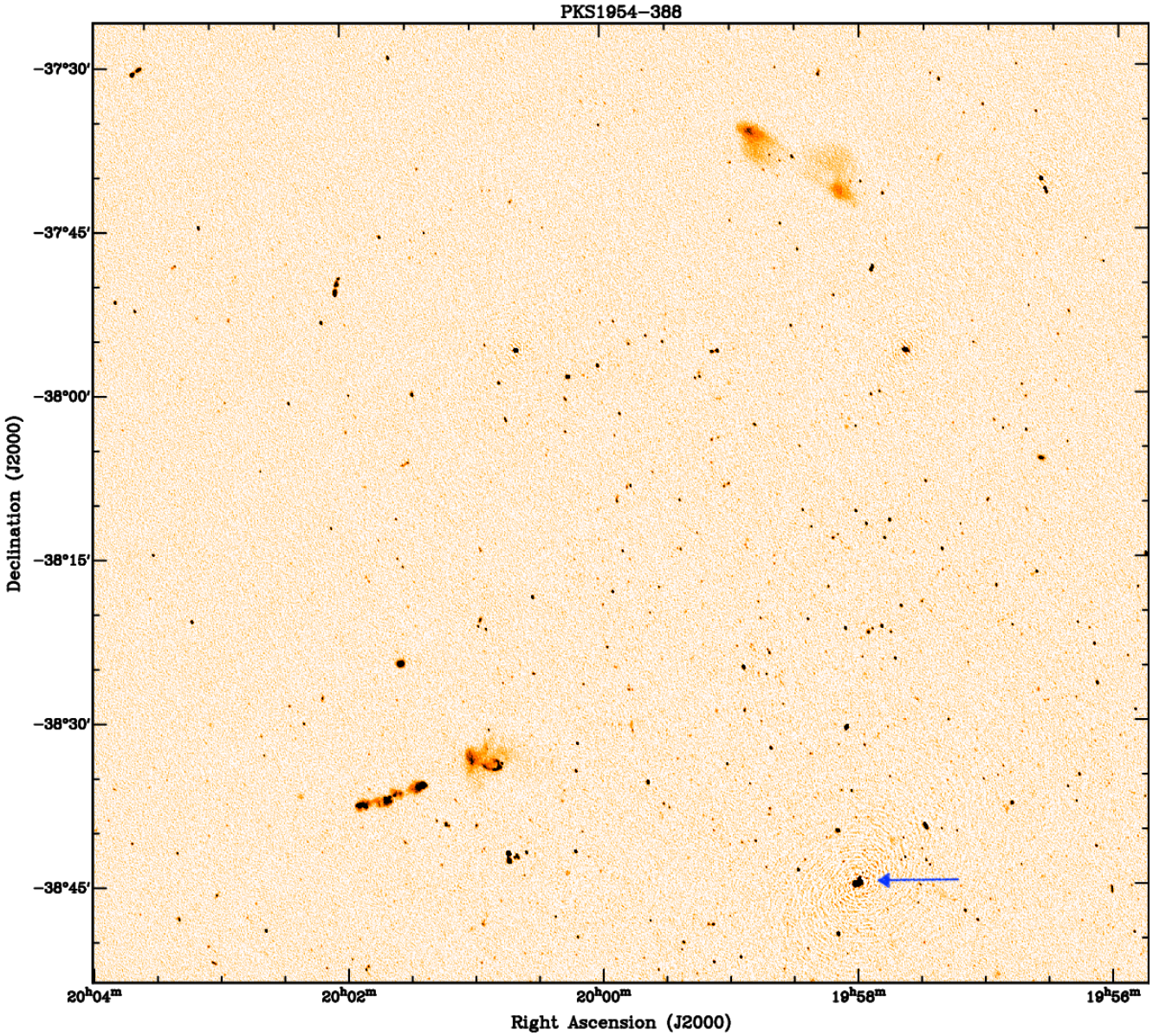

Fig. 2. Example of one of the continuum images obtained (PKS 1954–38), illustrating the image quality. The target, PKS 1954–38, is visible in the bottom of the image indicated with an arrow, and the residual artifacts around this source are due to the strength of the source. The total flux of PKS 1954–38 is 1.195 Jy and its peak is 940 mJy beam^{-1}. The root-mean-square level of the artefacts around PKS 1954–38 is 0.1 mJy beam^{-1} while the noise level away from the target is 0.05 mJy beam^{-1}. This indicates that the dynamic range near the target is about 10^4.

outflow is observed in PKS 1306–09. In this source, the fast outflow is aligned with the direction of the radio plasma and has comparable extent. The emission lines are broad (the FWHM of the [O III]λ5007 line is $\sim$1000 km s^{-1}) and double-peaked, with the blueshifted component of [O III]λ5007 having a velocity of $\sim$500 km s^{-1}. The situation in PKS 1151–34 is more difficult to characterise because of the presence of broad permitted emission lines in the spectrum. However, in both cases the (outflowing) ionised gas appears to be characterised by high densities (log $n_e \sim 3-4$ cm^{-3}). All this suggests the presence of an interaction between jets and gas – often seen in young radio sources – which could result in compression of the gas by jet-induced shocks.

The H I absorption profiles of the two sources show different characteristics which are discussed below. Both sources are particularly strong in radio continuum (about 7 and 5 Jy, respectively), while the H I absorbed flux is faint. The detection of such faint absorptions (especially in PKS 1306–09) confirms the good quality and stability of the bandpass of the MeerKAT telescope (more details are given in Appendix B).

5.1.1. A young quasar: PKS 1151–34

In PKS 1151–34, we detected H I absorption with a broad profile (W_{50} = 157 km s^{-1} and W_{20} = 350 km s^{-1}) and peak optical depth of only $\tau_{\rm peak}$ = 0.004. The absorption profile is roughly centred on the systemic velocity, but it is asymmetric in intensity, with the deeper peak on the blueshifted side (blueshifted by 79 ± 2 km s^{-1}). The asymmetry does not appear to be due to the presence of RFI on the redshifted side of the spectrum (although the exact width on the redshifted size could be affected by the RFI). However, it is more likely that it represents the shape resulting from the distribution of the gas

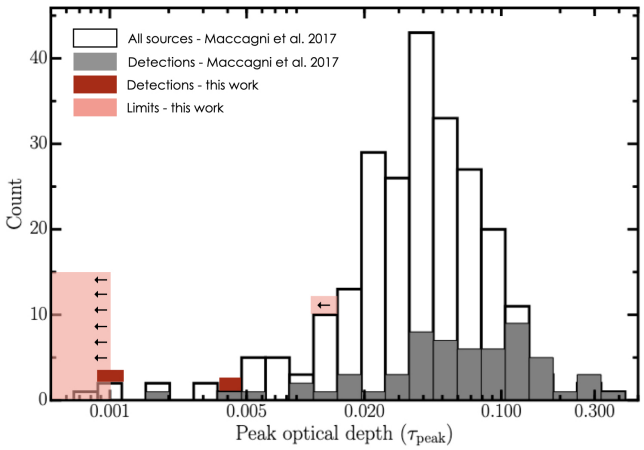

Fig. 3. Distribution of the peak optical depth taken from Maccagni et al. (2017, grey and empty bars) with overlaid the peak optical depth for the detected (dark red boxes) and limits thereof (light red) for the sources of the present sample. The distribution shows how the present observations reach very low optical depths.

combined with the morphology of the background continuum (see below).

As mentioned above, PKS 1151–34 is a young radio source. This is indicated by the steep spectrum, combined with the radio morphology and size. The radio spectrum is steep at high frequencies (with spectral index $\alpha_{8\,\mathrm{GHz}}^{2.7\,\mathrm{GHz}} = -0.7$, defined through $S \propto \nu^{\alpha}$, with S the continuum flux; see Tzioumis et al. 2002) with a flattening at lower frequencies, possibly indicating the separation between optically thin and thick emission. The source has a double-lobed structure with a total projected extent of about 680 pc. The VLBI image taken from Tzioumis et al. (2002) is shown in Fig. 4 (top-right). Neither of the two VLBI components shows the flat type of spectrum that would otherwise be typical of a core. These properties support the scenario in which the source is small because it is young (and not because of any extreme orientation or beaming effects, also considering the relatively symmetric lobes), despite the optical classification.

At optical wavelengths, PKS 1151–34 has been classified as a broad-line radio galaxy based on the detection of broad Balmer lines of moderate strength, although its [O III]λ5007 emission-line luminosity is more consistent with that of a quasar (Santoro et al. 2020). The clear presence of stellar absorption lines in its nuclear spectrum and the relatively red colours suggest that its AGN nucleus may be partially obscured at optical wavelengths.

The H I absorption could originate from the radio source being embedded in a circumnuclear gas disc. This is suggested by the fact that the absorption is roughly centred on the systemic velocity and by the shape of the absorption with a sharp edge of the profile on the blueshifted side, similar to those seen in emission for rotating discs and rings. The asymmetry in intensity could be due to the orientation of the radio source relative to the disc and ring, as schematically shown in the cartoon in Fig. 7. In this scenario, the deeper, blueshifted absorption would originate from the lobe located in the background (i.e. crossing a larger layer of gas). If the H I profile is due to gas rotating in a disc, the observed width of the profile ($W_0 = 450\,\mathrm{km\,s^{-1}}$) at a radius of 340 pc (i.e. the location of the radio lobes) can be explained by a central mass of the order of $4 \times 10^9\ M_\odot$ (without considering the effect of inclination). The mass of the BH in the centre of PKS 1151–34 can be estimated from the stellar mass-black hole mass relation (e.g. Kormendy & Ho 2013). The upper limit to the stellar mass (uncorrected for AGN contamination of the K-band luminosity) is $4 \times 10^{11}\ M_\odot$, as derived by Bernhard et al. (2022). This results in an upper limit to the BH mass of $2.5 \times 10^9\ M_\odot$. Thus, given the uncertainties, the rotation of the gas can be sustained by the central mass. The full confirmation of this scenario would require the location of the H I absorption in the radio lobes to be spatially resolved. Furthermore, the presence of gas with kinematics deviating from regular rotation, such as in- or outflowing clumps of gas, cannot be excluded. For this, observations with the southern VLBI array (Australian Long Baseline Array, LBA) reaching the frequency of H I at the redshift of PKS 1151–34 (i.e. 1129.09 MHz) will be needed.

Pinpointing the location of the absorption will also clarify whether all the H I is part of a regularly rotating structure or whether turbulent gas motions are also present (as hinted at by the broad absorption profile), possibly due to the jet interacting with the gas, as in the case of 4C 31.04 (Murthy et al. 2024), and/or resulting from gas settling following accretion from a companion galaxy. This source has not been observed by GALEX (it is outside the area covered by GALEX). However, thanks to the X-shooter observations of Santoro et al. (2020), the UV luminosity could be estimated (see Appendix A). This was done by extrapolating the measured fluxes from the Xshooter spectra at rest-frame wavelengths ~2200 – 2700 Å to 1216 Å using the Vanden Berk et al. (2001) mean quasar SED. Such an extrapolation is uncertain, given the (likely significant) contribution of starlight in the near UV. Therefore, the derived luminosity should be considered an upper limit. The UV luminosity derived in this way is $L_{\mathrm{UV}} = 1.8 \times 10^{22}\,\mathrm{W\,Hz^{-1}}$, which is below the limit proposed by Curran et al. (2008); therefore, the UV radiation is not expected to be hostile to the presence of H I. However, PKS 1151–34 is a strong radio source and, as described in the introduction, this can also have an effect on the conditions of the gas and, in particular, on the T_{spin}, which, in turn, affects the observed optical depth. To illustrate the possible impact of this, we can use the formulae presented in Bahcall & Ekers (1969) to estimate the T_{spin}[1]. The results are shown in Fig. 8 where we plot T_{spin} as function of H I volume density for two scenarios. Based on the idea of the radio lobes being embedded in the gas disc (Fig. 7), we have considered two extreme cases: (i) the gas is located in a disc at an average distance of 340 pc (half the size of the radio source) and affected by the flux of one of the lobes, namely ~3.5 Jy, half of the total flux (solid line in Fig. 8); (ii) the gas is located at a distance of 1 kpc, corresponding to the de-projected radius for a viewing angle of 20° (solid line). The plot of Fig. 8 (obtained under the conservative assumption of the kinetic temperature $T_{\mathrm{kin}} = 100$ K) shows that in either of the two cases (and for any realistic value of the H I volume density), the T_{spin} is high, possibly up to a few thousand K (i.e. well above the conventional 100 K). High T_{spin} values ($\gtrsim$1000 K) are consistent with those obtained, using the extinction estimates derived from the optical continuum modelling, in the case of the 2-Jy quasar PKS 1549–79, for which a T_{spin} in the range $3000 < T_{\mathrm{spin}} < 6000$ K was found (see Holt et al. 2006 for details). Also in this case, VLBI observations will be needed to derive more accurate parameters (T_{spin} and $n_{\mathrm{H\,I}}$) for PKS 1151–34.

For $T_{\mathrm{spin}} = 1000$ K (and a covering factor of unity) in the case of PKS 1151–34, we derived a column density of $N_{\mathrm{H\,I}} =$

[1] Note that a theoretical upper limit of 8000 K has been estimated by Maloney et al. (1996) above which all H I is expected to be ionised.

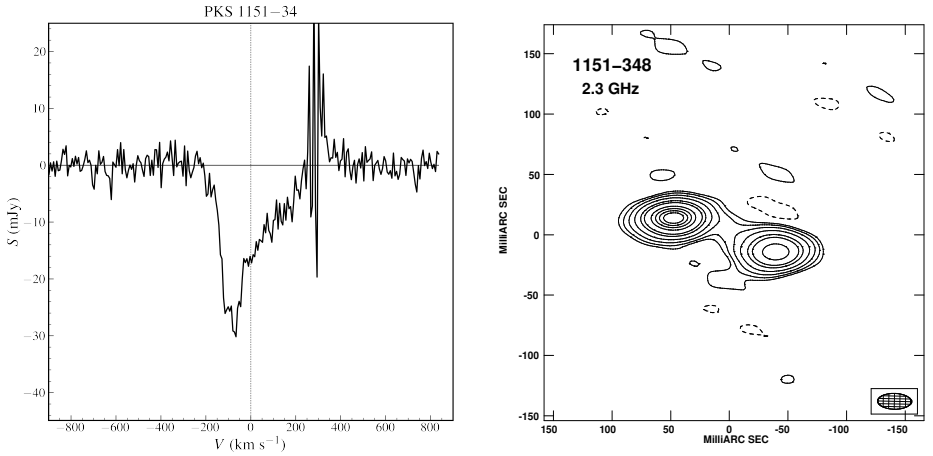

Fig. 4. Left panel: H I absorption profile in PKS 1151–34. Note: the RFI affecting part of the band. The error in the zero-point of the velocity scale is 30 km s^{-1} (see Table 1). Right panel: VLBI image of PKS 1151–34 from Tzioumis et al. (2002). The continuum emission spans ~700 pc.

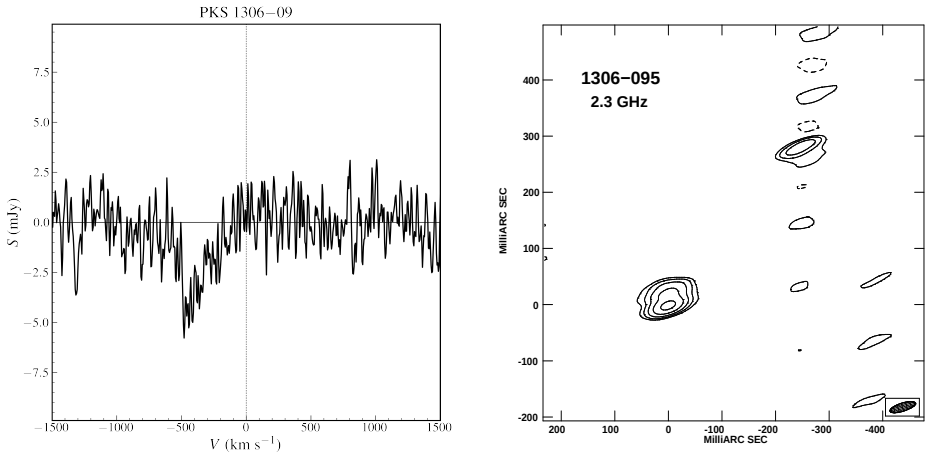

Fig. 5. Left panel: H I absorption profile against the young radio galaxy PKS 1306–09. The error in the zero-point of the velocity scale is 20 km s^{-1} (see Table 1). Right panel: VLBI image of PKS 1306–09 taken from Tzioumis et al. (2002). The size of the continuum emission is 2.4 kpc.

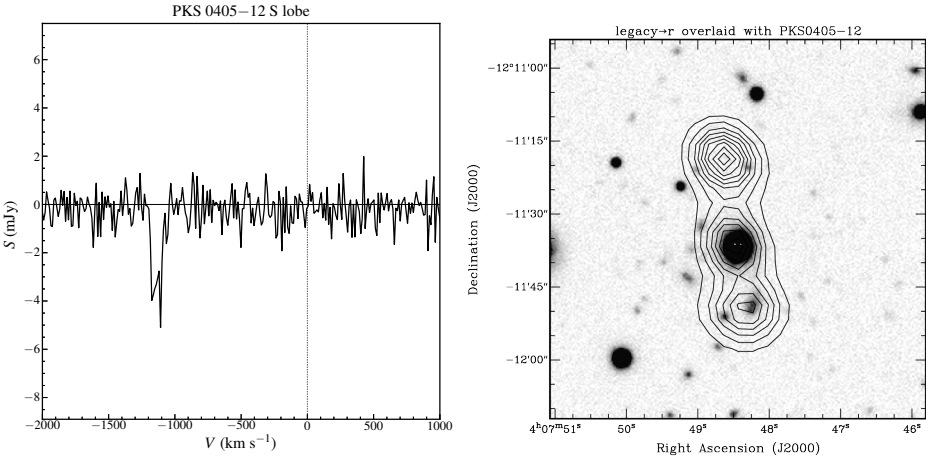

Fig. 6. Left panel: H I absorption detected against the southern lobe of PKS 0405–12 where an optical galaxy is also visible. Right panel: Continuum image of PKS 0405–12 superposed to the optical *r*-band image of PKS 0405–12 from DESI Legacy Imaging Surveys (Dey et al. 2019).

1.3×10^{21} cm^{-2}, which is not overly extreme and similar to what has been obtained for other radio sources (Morganti & Oosterloo 2018). Thus, in this source, the UV luminosity is low, consistent with atomic neutral hydrogen being present close to the active SMBH. However, the $T_{\rm spin}$ of the gas is likely high, which explains the low optical depth of the H I observed in this object.

Finally, despite the confirmed presence of atomic hydrogen, no CO(1–0) has been detected with ALMA in this source (Tadhunter et al. 2024). However, in agreement with the H I detection, the Herschel observations from Bernhard et al. (2022) and Dicken et al. (2023) have shown evidence of a substantial cool ISM (~$10^{7.5}$ $M_{\odot}$ of dust). Thus, the non-detection of CO(1-0) could indicate that the cold molecular gas has extreme conditions, such as a high excitation temperature, resulting in the high J-transitions being more luminous compared to CO(1–0). This has been seen now in a number of cases (see e.g. Oosterloo et al. 2025 and refs therein, and Oosterloo et al. in prep.).

The presence of a rich medium in PKS 1151–34 is also suggested by the evidence of an interaction with a nearby companion galaxy affecting the PKS 1151–34 host. This interaction is clearly indicated by the second nucleus and distorted structures visible in the optical image of Ramos Almeida et al. (2011). Xshooter observations (Santoro et al. 2020) have

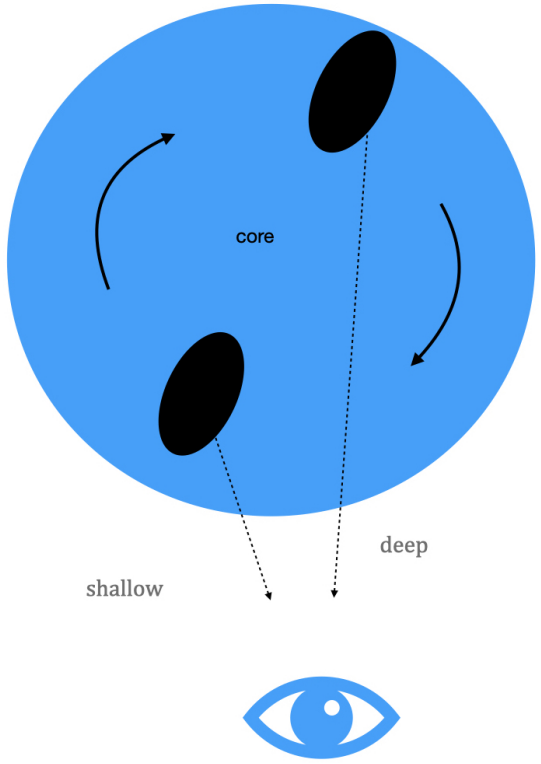

Fig. 7. Cartoon of the possible geometry explaining the absorption in the young quasar PKS 1151–34 (Sect. 5.1.1).

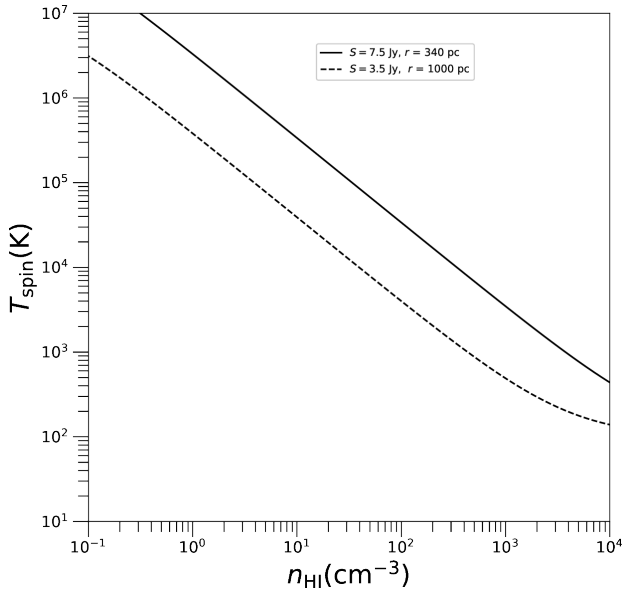

Fig. 8. Estimated $T_{\rm spin}$ as function of the column density derived for PKS 1151–34 following the calculation in Bahcall & Ekers (1969); see Sect. 5.1.1 for details. The plot shows that high values of $T_{\rm spin}$ are expected for the typical densities of the H I clouds.

confirmed that the second nucleus has a redshift close to that of the target (see Appendix C for further details).

5.1.2. H I in a young radio galaxy: PKS 1306–09

Similar to the case of PKS 1151–34, PKS 1306–09 is a young radio source. The radio continuum structure shows two lobes and a total projected size of about 2.4 kpc (see Fig. 5 right). PKS 1306–09 has a steep spectrum at high frequencies ($\alpha_{8\ \rm GHz}^{2.7\ \rm GHz} = -0.85$, Tzioumis et al. 2002). Its size is consistent with those found for other CSS and with the lack of a flattening or peak at low frequencies (O'Dea & Saikia 2021). As for PKS 1151–34, these properties support the scenario in which the source is small because it is young, and not because of orientation or beaming effects.

In this source, we detected an absorption with extremely low optical depth ($\tau_{\rm peak} = 0.0009$). Considering the strength of the source (5.4 Jy), this again illustrates the excellent spectral stability of MeerKAT. As in the case of PKS 1151–34, the absorption profile is broad $W_{20} = 405\,{\rm km\,s^{-1}}$. However, in PKS 1306–09 the H I profile appears highly blueshifted, by almost 500 $\rm km\,s^{-1}$ compared to the systemic redshift derived by Santoro et al. (2020). In addition, the width of the H I profile is large ($\sigma = 110\,{\rm km\,s^{-1}}$) suggesting that the gas is not quiescent. Thus, it is unlikely that the H I is associated with a rotating disc. Instead, the H I could be part of the gas outflow which has been identified using X-shooter (Santoro et al. 2020) in the warm ionised gas. The broad [O III]λ5007 emission line tracing this outflow has been found to be extended in the same direction as the radio emission, suggesting a possible jet-driven outflow. Furthermore, the optical [O III]λ5007 emission-line profile is double-peaked and the blue peak has a velocity ($\sim -500\,{\rm km\,s^{-1}}$) that is close to that of the H I absorption. Thus, the detection of H I with similar blueshifted velocities at the location of the radio emission reinforces the scenario that cold gas (H I) is also associated with the outflow and that the outflow is being driven by the radio jets. This expands the number of cases, especially in young radio galaxies, where multi-phase outflows are observed, including gas in the cold phase (atomic neutral hydrogen and molecular; Morganti & Oosterloo 2018 and refs. therein; Murthy et al. 2024).

We can estimate the mass outflow rate ($\dot{M}$) using the expression from Heckman et al. (2002), expressed as

$$\dot{M} = 30 \frac{\Omega}{4\pi} \times \frac{r_*}{1\,{\rm kpc}} \times \frac{N_{\rm H\,I}}{10^{21}\,{\rm cm^{-2}}} \times \frac{v}{300\,{\rm kms^{-1}}}\ M_\odot\ {\rm year^{-1}}, \quad (1)$$

where Ω is the solid angle the outflow subtends (which we assume to be π), r_* is the radius of the outflow, assumed to be 1.2 kpc (half of the source extent), $N_{\rm H\,I}$ is the column density of 0.4×10^{21} $\rm cm^{-2}$ estimated with the conservative assumption of $T_{\rm spin} = 1000$ K and assuming the H I covers the entire source, $c_{\rm f} = 1$. This results in a mass outflow rate $\dot{M} = 2.5$ $M_\odot\ {\rm yr^{-1}}$. Although not extreme, this is consistent with what has been found for H I outflows in other radio AGNs (see Table 1 in Morganti & Oosterloo 2018). Interestingly, this is also consistent with the outflow of warm ionised gas described in Santoro et al. (2020), where two approaches were used to estimate the mass outflow rate of the warm gas, resulting in lower limits between 0.4 and 1.4 $M_\odot\ {\rm yr^{-1}}$.

As for PKS 1151–34, no UV detection from GALEX is available for PKS 1306–09. Therefore, the UV luminosity was estimated from the extrapolation of the X-shooter fluxes in the same way as for PKS 1151–34 (see Appendix A). The resulting UV luminosity is low, $L_{\rm UV} = 8 \times 10^{21}\,{\rm W\,Hz^{-1}}$ at 1216Å, again below the limit proposed by Curran et al. (2008) and suggesting conditions favourable for H I to be detected. However, as in the case of PKS 1151–34, the high radio flux of the small radio source, together with the likely presence of jet-ISM interactions, suggest that in this source the gas could have a high $T_{\rm spin}$ (i.e. $\gtrsim$1000 K), which could be the reason for the low optical depth observed.

5.2. Local intervening case

In one object, PKS 0405–12, the spectrum reveals H I absorption at the location of the southern lobe (see Fig. 6). The absorption is blueshifted by ~1100 km s^{-1} with respect to the systemic velocity of PKS 0405–12 (z = 0.574). The derived column density is 0.8 × 10^{18} $T_{\rm spin}/c_{\rm f}$. The offset in velocity and the off-centre location indicate a situation different from that in the other two sources. The overlay of the radio continuum on the optical image (Fig. 6 left) shows that a companion galaxy is located, in projection, about 100 kpc from PKS 0405–12, against the southern radio lobe where the absorption was detected. Thus, the absorption appears to be caused by this galaxy, which was identified by Marr & Spinrad (1985) as a large spiral galaxy[2] with strong [O II] emission lines at a redshift of z = 0.5678. PKS 0405–12 is located in a group or cluster environment and this intervening galaxy appears to be part of this local environment. Thus, we consider the H I detected to be an example of 'local intervening absorption'.

Such off-nucleus local-intervening H I absorptions are not very common, but a few cases are known. In two of these, the absorption appears to be associated with a giant gas disc not located close to the nucleus, but still associated with the host galaxy itself. Coma A (Morganti et al. 2002) is the clearest case, while PKS 1649–062 (Curran et al. 2011) is a possible other example.

An instance that is even more similar to the case of PKS 0405–12 relates the H I absorption features associated with galaxies located in the foreground of some radio sources. For example, H I absorption from a small companion disc galaxy has been observed against the radio lobe of 3C 433 (Murthy et al. 2020). The column density measured in that case (1 × 10^{18} cm^{-2} $T_{\rm spin}$) is similar to the one detected in PKS 0405–12. Against the radio lobe of another source in the 2-Jy sample, PKS 0409–75, Mahony et al. (2022) have found absorption blueshifted by ~3300 km s^{-1} compared to the optical redshift of the host galaxy and with a column density of 2.16 × 10^{21} cm^{-2}, assuming a spin temperature of $T_{\rm spin}$ = 500 K and covering factor of $c_{\rm f}$ = 0.3. This would correspond to 1.3 × 10^{18} ($T_{\rm spin}/c_{\rm f}$), comparable to what found for PKS 0405–12.

The width of the absorption (W_{20} = 125 km s^{-1}) is narrower compared to those measured for the associated absorptions found in the present sample. This is, to first order, consistent with what is expected for intervening H I absorption (see Curran 2021 for a discussion). However, the profile is relatively broad for an intervening absorber, with W_0 ~ 160 km s^{-1}, likely because the absorption is observed against an extended continuum source. This suggests that some of the spread in rotational velocity of the gas in the spiral galaxy is included. This can complicate the separation between associated and intervening absorbers based only on the width of the profile (see below).

6. Origin and properties of the H I absorbers

In this work, we present observations searching for H I absorption in a sample of powerful radio sources at intermediate redshift (0.25 < z < 0.7). The observations took advantage of the capabilities and performance (broad and stable bandpass, limited RFI, etc.) of the MeerKAT radio telescope. Because of this, given the brightness of the sources of the sample, we have been able to reach extremely low optical depth ($\tau_{\rm peak} \ll 0.01$). Some of our findings are similar to what could be expected based on low-z studies and we find no indication of major changes in the H I properties at these intermediate redshift.

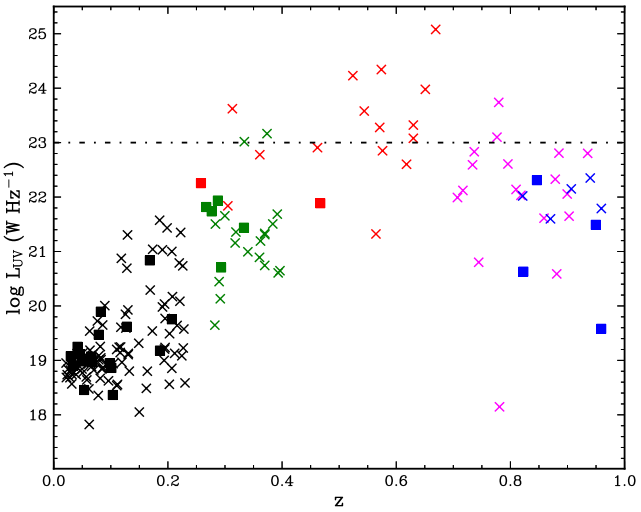

Fig. 9. UV luminosities for our sample (red points) together with some available in literature (black = Maccagni et al. (2017), green = Murthy et al. (2021), magenta = Murthy et al. (2022), and blue = Aditya (2019), adapted from Murthy et al. (2022). Square points are detections, crosses represent the limits. The dashed line represents the $L_{\rm UV}$ = 10^{23} W Hz^{-1} threshold proposed by Curran et al. (2008, see text for details).

For 15 objects, we obtained useful H I spectra (i.e. free from RFI), with three H I absorptions detected, two associated absorptions in young radio sources and one so-called local intervening system against the lobe of one of the extended radio sources and associated with a foreground galaxy. Thus, despite the high sensitivity, we obtained a relatively low detection rate of associated absorption (i.e 13% ± 7%), albeit with a large uncertainty. The low detection rate is not completely surprising given that the sample includes mostly core dominated sources with broad optical emission lines, typical of quasar hosts. According to the unified schemes, dust and gas absorption are mostly due to the circumnuclear torus and disc, which (in the case of these AGN types) are oriented close to face-on. Therefore, these AGNs are expected to be mostly unobscured. In this respect, the low detection rate can be attributed to the geometry of the absorber.

However, as described in the introduction, other effects can influence the detection rate, and one of the important parameters is the UV luminosity. Figure 9 shows the distribution of the UV luminosities derived as described in Appendix A. About half of the sample has a luminosity above $L_{\rm UV}$ = 10^{23} W Hz^{-1}, namely, the threshold proposed by Curran et al. (2008) as the limit above which H I can be ionised by the strong UV radiation. In agreement with this, we have no H I detections among those sources. However, below this limit, associated H I absorption has been detected for only two sources. Therefore, although it is difficult to completely distinguish between orientation and UV luminosity playing an important role in whether the H I absorption might be detected, our results suggest that the UV luminosity is not the only parameter influencing the H I detection and that the orientation is also an important parameter.

The optical depths of the H I we observe are very low. Such low values could be reached because the target sources are strong and we obtained sensitive and high-quality observations. In the case of our sources, the low optical depth could be the result of the gas having a high $T_{\rm spin}$ due to the combination of the gas

[2] Coordinates RA: 04$^{\rm h}$ 07$^{\rm m}$ 48$^{\rm s}$.2, Dec: –12°11′48″.9 (J2000).

being located in the vicinity of the active black hole and the strong radio flux. We show this for the case of one of the detections (PKS 1151–34). Thus, our results suggest that in general, the detection rate of H I absorption should be interpreted with care, because it is strongly dependent on the properties of the studied sample and the depth of the observations. Well characterised samples and observations reaching low optical depth are needed to get a complete inventory of the presence of H I.

Notably, we find that both detections of associated H I are in young radio sources (i.e. two of the four CSS and peaked sources in our sample were detected). This confirms the trend seen both at low and high redshifts (see Sect. 1) and we see that even at intermediate redshift, they represent the most frequently detected sources in H I. This trend is also starting to emerge from blind H I absorption surveys such as FLASH (Yoon et al. 2025).

The richness of the ISM observed in these sources is likely to be an important factor in their H I detectability. Based on the detected level of star formation activity and the amount of dust and cold molecular gas (see O'Dea & Saikia 2021; Dicken et al. 2023; Tadhunter et al. 2024 and refs therein), there is now considerable evidence that CSS and GPS have a richer ISM than their more extended counterparts. Interestingly, the presence of gas and the likely presence of interactions between jet and ISM, could, in fact, boost their radio emission and explain the large number of such sources detected in radio surveys (see Morganti et al. 2011 for details). In addition to the gas, the fact that the size of the radio source matches that of the distribution of the gas in the circumnuclear regions could further help in boosting the detectability of these sources in H I.

In the context of the type of bias introduced by the selection of the sources in the present sample, the case of the one broad-line, quasar-like object in our sample detected in H I (PKS 1151–34) is interesting. On the basis of the orientation-based unified schemes for radio AGNs, we would expect the nucleus of this broad-line object to be relatively unobscured. Nevertheless H I absorption has indeed been detected. For this quasar, which is classified as a young radio source, we suggest (based on the H I profile, which is centred on the systemic velocity but highly asymmetric with the blueshifted peak much deeper) that the gas is distributed in a disc or ring with the radio source (two lobes with a projected size of 680 pc) still embedded in it (see Fig. 7 for the proposed scenario). Thus, the nucleus may be partially obscured by this structure. Indeed, this is what is suggested by the presence of stellar absorption lines in its nuclear optical spectrum and the relatively red colours (Santoro et al. 2020), indicating that a more complex situation than the standard circumnuclear torus and disc predicted from the unified scheme can be at work.

The $T_{\rm spin}$ in PKS 1151–34 is likely to be high, around 4000 K. This could explain the low optical depth of the detected gas ($\tau_{\rm peak}$ = 0.004). If these conditions are also present in other sources, they could, as mentioned above, affect the detection fraction of in observations of limited sensitivity.

In the second associated detection, PKS 1306–09, the H I is found to be significantly blueshifted (~500 km s^{-1}) compared to the systemic velocity. Also, in this object, the H I profile is broad (with velocity dispersion around 100 km s^{-1}) and has a low optical depth ($\tau_{\rm peak}$ = 0.0009). This is another case that would be missed by shallow surveys. The large blueshifted velocity and the agreement found for the warm ionised gas (see Sect. 5.1.2 and Santoro et al. 2020) suggest that the H I is part of a fast outflow, likely driven by the jet-ISM interaction. Although we cannot pinpoint the location of this blueshifted component (due to the limited resolution of our observations), we know that the lobes of the radio source are about 2 kpc apart, suggesting that the H I (if it is indeed interacting with the radio plasma) is on those scales. This finding expands on the number of young (or restarted) radio AGNs, where outflows of cold gas (atomic neutral hydrogen and cold molecular gas) are found. This also confirms the predictions of simulations of the impact of the initial phase of the young radio jet on the surrounding medium, which is traced by the presence of gas outflows and large velocity dispersion of the gas due to the creation of a cocoon of shocked gas around the jet (Mukherjee et al. 2018 and refs therein).

In contrast to the two associated absorption detections, a third absorption detection originates in an intervening companion galaxy located in front of the radio lobe of PKS 0405–12. The galaxy is likely part of the galaxy group surrounding the central quasar (with a difference in velocity of ~1100 km s^{-1}); therefore, we have defined it as a local intervening case. Interestingly, this absorption has a narrower profile compared to the associated ones. Curran (2021) has proposed to use the width of the H I profile as a criterion to separate associated from intervening absorption in large blind H I absorption surveys. However, according to Curran (2021), only for FWZI $\leq$ 50 km s^{-1} there is a ~90 per cent probability of the absorber being intervening. For cases of local intervening absorption such as PKS 0405–12, the broader profile (FWZI ~ 160 km s^{-1}) is likely due to the inclusion of some of the rotation of the gas in the intervening galaxy because the absoprtion is observed against an extended continuum background. This is relevant because it indicates that for blind surveys, it will be difficult to classify a group of H I profiles as 'associated' or 'intervening', unless the radio data are characterised by a good spatial resolution and/or complementary optical data are available to identify these situations.

7. Conclusions

Thanks to the well-characterised sources and deep radio observations, the sample of radio AGN targets of this study has shown a variety of H I absorption properties, similarly to what has been found for low-z objects, such as the low-z part of the 2 Jy sample presented in Morganti et al. (2001). The sample presented here is dominated by broad-line sources where, according to the unified schemes, the nucleus should be unobscured. Indeed, we do have a relatively low detection rate (13% ± 7%), with the majority of the sources are not detected, even if the UV luminosity is below the limit of 10^{23} W Hz^{-1}.

However, young (CSS and peaked) radio sources, also at intermediate redshifts, are confirmed to be more likely to be detected, even in the case where they are quasars. It is, however, important to note that the two detections have extreme low optical depths ($\tau_{\rm peak} < 0.005$) and could only be found thanks to the depth and stability of the MeerKAT observations presented here. The higher occurrence of H I in CSS and peaked sources is often considered to be related to the richness of their ISM and the results from our study further confirm this. This highlights the need for ancillary data to complement the H I observations. This is important for the blind surveys such as FLASH (Yoon et al. 2025), which are now expanding the view of atomic neutral hydrogen in AGNs to higher redshifts.

In general, the results (i.e. detection rate and properties of the absorption) for the present study, which is focussed on well characterised (at multi-wavelengths) target sources, can guide the interpretation of the results from untargeted surveys. Follow-up H I high-resolution (VLBI) observations are needed to confirm the scenarios we propose about the distribution of the absorber in PKS 1151–34 and the presence of an H I outflow in PKS

1306–09. The VLBI capability of SKA will be an extremely valuable addition to trace the HI on parsec scales. At the same time, observations of multiple transitions of the molecular gas observed in emission (e.g. CO) would help to elucidate more information on the full distribution and physical conditions of the gas, overcoming the limitations of absorption studies.

The sample presented here is still biased towards core-dominated objects and against extended, FRII-like, sources. Expanding to the latter group of objects will be the next step to test the presence of circumnuclear H I discs as main absorber in radio AGNs, thereby reinforcing the role of orientation in the detection rate of H I absorption. However, such observations will prove to be time-consuming because the cores of these sources typically exhibit low radio flux. In general, the present study shows that the limitations of the studied samples, in terms of selecting the targets and depth of the observations, should be taken into account when interpreting the detection rate and the properties of the H I gas in radio AGNs.

Acknowledgements. The MeerKAT telescope is operated by the South African Radio Astronomy Observatory, which is a facility of the National Research Foundation, an agency of the Department of Science and Innovation. This work used images from the DESI Legacy Imaging Surveys (Dey et al. 2019). Their full acknowledgment is at https://www.legacysurvey.org/acknowledgment/.

References

Aditya, J. N. H. S. 2019, MNRAS, 482, 5597
Aditya, J. N. H. S., & Kanekar, N. 2018a, MNRAS, 481, 1578
Aditya, J. N. H. S., & Kanekar, N. 2018b, MNRAS, 473, 59
Aditya, J. N. H. S., Kanekar, N., & Kurapati, S. 2016, MNRAS, 455, 4000
Aditya, J. N. H. S., Kanekar, N., Prochaska, J. X., et al. 2017, MNRAS, 465, 5011
Aditya, J. N. H. S., Jorgenson, R., Joshi, V., et al. 2021, MNRAS, 500, 998
Aditya, J. N. H. S., Yoon, H., Allison, J. R., et al. 2024, MNRAS, 527, 8511
Audibert, A., Dasyra, K. M., Papachristou, M., et al. 2022, A&A, 668, A67
Bahcall, J. N., & Ekers, R. D. 1969, ApJ, 157, 1055
Bernhard, E., Tadhunter, C. N., Pierce, J. C. S., et al. 2022, MNRAS, 512, 86
Burgess, A. M., & Hunstead, R. W. 2006, AJ, 131, 114
Callingham, J. R., Ekers, R. D., Gaensler, B. M., et al. 2017, ApJ, 836, 174
Chandola, Y., Sirothia, S. K., & Saikia, D. J. 2011, MNRAS, 418, 1787
Chandola, Y., Gupta, N., & Saikia, D. J. 2013, MNRAS, 429, 2380
Cheng, X.-P., An, T., Frey, S., et al. 2020, ApJS, 247, 57
Cheng, X., An, T., Wang, A., et al. 2023, Galaxies, 11, 42
Crain, R. A., & van de Voort, F. 2023, ARA&A, 61, 473
Curran, S. J. 2021, MNRAS, 506, 1548
Curran, S. J., Whiting, M. T., Wiklind, T., et al. 2008, MNRAS, 391, 765
Curran, S. J., Whiting, M. T., Webb, J. K., et al. 2011, MNRAS, 414, L26
Curran, S. J., Whiting, M. T., Sadler, E. M., et al. 2013, MNRAS, 428, 2053
Curran, S. J., Whiting, M. T., Allison, J. R., et al. 2017, MNRAS, 467, 4514
Dey, A., Schlegel, D. J., Lang, D., et al. 2019, AJ, 157, 168
Dicken, D., Tadhunter, C. N., Nesvadba, N. P. H., et al. 2023, MNRAS, 519, 5807
Dijkema, T. J., Nijhuis, M., van Diepen, G., et al. 2023, Astrophysics Source Code Library [record ascl: 2305.014]
Dutta, R., Kurapati, S., Aditya, J. N. H. S., et al. 2022, J. Astrophys. Astron., 43, 103
Dutta, R., Sharma, P., Sarkar, K. C., et al. 2024, ApJ, 973, 148
Fernini, I. 2014, ApJS, 212, 19
Geréb, K., Maccagni, F. M., Morganti, R., et al. 2015, A&A, 575, A44
Glowacki, M., Allison, J. R., Sadler, E. M., et al. 2017, MNRAS, 467, 2766
Gupta, N., Salter, C. J., Saikia, D. J., et al. 2006, MNRAS, 373, 972
Heckman, T. M., Norman, C. A., Strickland, D. K., et al. 2002, ApJ, 577, 691
Holt, J., Tadhunter, C., Morganti, R., et al. 2006, MNRAS, 370, 1633
Holt, J., Tadhunter, C. N., & Morganti, R. 2008, MNRAS, 387, 639
Kanekar, N., & Briggs, F. H. 2004, New Astron. Rev., 48, 1259
Kormendy, J., & Ho, L. C. 2013, ARA&A, 51, 511
Lister, M. L., Cohen, M. H., Homan, D. C., et al. 2009, AJ, 138, 1874
Maccagni, F. M., Morganti, R., Oosterloo, T. A., et al. 2017, A&A, 604, A43
Maccagni, F. M., Morganti, R., Oosterloo, T. A., et al. 2018, A&A, 614, A42
Maccagni, F. M., Ruffa, I., Loni, A., et al. 2023, A&A, 675, A59
Mahony, E. K., Allison, J. R., Sadler, E. M., et al. 2022, MNRAS, 509, 1690
Maloney, P. R., Hollenbach, D. J., & Tielens, A. G. G. M. 1996, ApJ, 466, 561
Marr, J., & Spinrad, H. 1985, PASP, 97, 684
McMullin, J. P., Waters, B., Schiebel, D., Young, W., & Golap, K. 2007, ASP Conf. Ser., 376, 127
Morganti, R. 2024, IAU Symp., 392, 10
Morganti, R., & Oosterloo, T. 2018, A&ARv, 26, 4
Morganti, R., Killeen, N. E. B., & Tadhunter, C. N. 1993, MNRAS, 263, 1023
Morganti, R., Oosterloo, T., Tadhunter, C. N., et al. 1999, A&AS, 140, 355
Morganti, R., Oosterloo, T. A., Tadhunter, C. N., et al. 2001, MNRAS, 323, 331
Morganti, R., Oosterloo, T. A., Tinti, S., et al. 2002, A&A, 387, 830
Morganti, R., Oosterloo, T. A., Emonts, B. H. C., et al. 2003, ApJ, 593, L69
Morganti, R., Tadhunter, C. N., & Oosterloo, T. A. 2005, A&A, 444, L9
Morganti, R., Peck, A. B., Oosterloo, T. A., et al. 2009, A&A, 505, 559
Morganti, R., Holt, J., Tadhunter, C., et al. 2011, A&A, 535, A97
Mukherjee, D., Bicknell, G. V., Wagner, A. Y., et al. 2018, MNRAS, 479, 5544
Murthy, S., Morganti, R., Emonts, B., et al. 2020, A&A, 643, A74
Murthy, S., Morganti, R., Oosterloo, T., et al. 2021, A&A, 654, A94
Murthy, S., Morganti, R., Kanekar, N., et al. 2022, A&A, 659, A185
Murthy, S., Morganti, R., Oosterloo, T., et al. 2024, A&A, 688, A84
O'Dea, C. P., & Saikia, D. J. 2021, A&ARv, 29, 3
Offringa, A. R., McKinley, B., Hurley-Walker, N., et al. 2014, MNRAS, 444, 606
Oosterloo, T., Morganti, R., Tadhunter, C., et al. 2025, A&A, 700, A22
Perucho, M. 2024, A&A, 684, A45
Ramos Almeida, C., Tadhunter, C. N., Inskip, K. J., Morganti, R., Holt, J., & Dicken, D. 2011, MNRAS, 410, 1550
Reid, R. I., Kronberg, P. P., & Perley, R. A. 1999, ApJS, 124, 285
Rose, T., McNamara, B. R., Combes, F., et al. 2024, MNRAS, 533, 771
Saintonge, A., & Catinella, B. 2022, ARA&A, 60, 319
Santoro, F., Tadhunter, C., Baron, D., et al. 2020, A&A, 644, A54
Schulz, R., Morganti, R., Nyland, K., et al. 2018, A&A, 617, A38
Schulz, R., Morganti, R., Nyland, K., et al. 2021, A&A, 647, A63
Serra, P., et al. 2012, MNRAS, 422, 1835
Struve, C., & Conway, J. E. 2010, A&A, 513, A10
Struve, C., & Conway, J. E. 2012, A&A, 546, A22
Tadhunter, C. 2008, New Astron. Rev., 52, 227
Tadhunter, C. 2016, A&ARv, 24, 10
Tadhunter, C. N., Morganti, R., di Serego Alighieri, S., Fosbury, R. A. E., & Danziger, I. J. 1993, MNRAS, 263, 999
Tadhunter, C. N., Morganti, R., Robinson, A., Dickson, R., Villar-Martín, M., & Fosbury, R. A. E. 1998, MNRAS, 298, 1035
Tadhunter, C., Dickson, R., Morganti, R., et al. 2002, MNRAS, 330, 977
Tadhunter, C., Oosterloo, T., Morganti, R., et al. 2024, MNRAS, 532, 4463
Tremblay, G. R., Oonk, J. B. R., Combes, F., et al. 2016, Nature, 534, 218
Tzioumis, A., King, E., Morganti, R., et al. 2002, A&A, 392, 841
van Gorkom, J. H., Knapp, G. R., Ekers, R. D., et al. 1989, AJ, 97, 708
Vanden Berk, D. E., Richards, G. T., Bauer, A., et al. 2001, AJ, 122, 549
Vermeulen, R. C., Pihlström, Y. M., Tschager, W., et al. 2003, A&A, 404, 861
Yoon, H., Sadler, E. M., Mahony, E. K., et al. 2025, PASA, 42

Appendix A: UV luminosities

The UV luminosities for the 2-Jy objects were obtained using different approaches depending on the data available. The luminosities were corrected to 1216 Å to make them consistent with Curran et al. (2008). No correction has been made for Galactic dust extinction.

A group of objects (PKS 0403–13, PKS 0405–12, PKS 0637–75, PKS 1136–13, PKS1954-388, PKS 2203–18, PKS 2243–12 and PKS 2345–16) were observed and detected with GALEX. For these objects we extrapolated down to 1216 Å assuming a power law and a spectral index derived from the NUV and FUV measurements.

A second group (PKS 0252–71, PKS 1151–54, PKS 1306–09), which include the two H I detected objects, is made of radio galaxies that were not detected nor observed by GALEX, but with VLT Xshooter observations (all CSS sources) from Santoro et al. (2020). In these cases, we extrapolated from the measured flux typically from the Xshooter spectra at rest-frame wavelength ~2200–2700 Å) to 1216Å using the Vanden Berk et al. (2001) quasar SED. The correction factor is typically quite large (2.4), so these are very much upper limits because use of the quasar SED is likely to substantially overestimate the true UV fluxes of these galaxies, for which the optical/UV light is likely to have a significant stellar component.

PKS1355–41 and PKS1510–08 were not observed by GALEX, but have been observed in the UV with HST/COS or IUE, covering the redshifted wavelength of Lymanα.

Finally a group of four objects (PKS0159–11, PKS0842–75, PKS0859–25 and PKS1602+01) have no observations in the UV. For these, we have taken the 3500Å (rest) fluxes from Tadhunter et al. (1993) of the optical spectra and extrapolated to 1216Å using the Vanden Berk et al. (2001) quasar SED. For these cases, the correction factor is large (4.2).

Appendix B: Bandpass stability of the observations of PKS 1306–09

To illustrate the good quality and stability of the bandpass calibration, we applied the bandpass calibration obtained using J0408–6545 which was observed at the end of the observing block used for PKS 1306–09, to the observation of PKS 1934–63 which was observed at the beginning of this observing block. The resulting spectrum (expressed in optical depth), is shown in Fig. B.1 and shows that this spectrum is noise dominated.

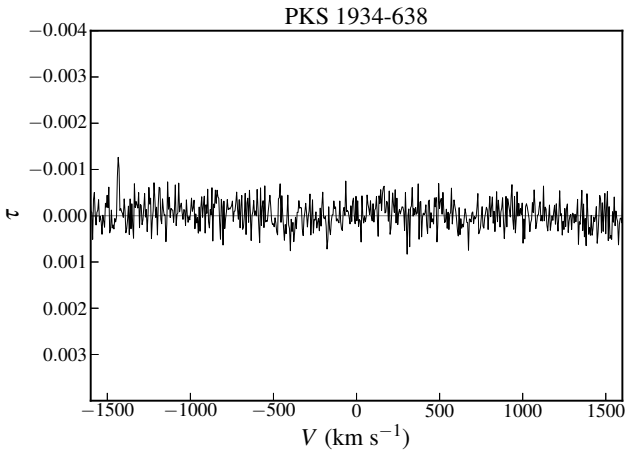

Fig. B.1. Spectrum of PKS 1934–63 calibrated using the bandpass derived from J0408–6545 observed several hours later.

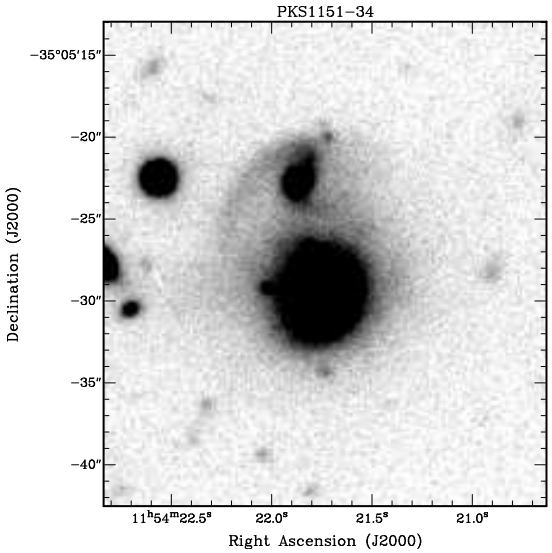

Fig. C.1. GMOS-S/Gemini optical broad-band image of PKS 1151–34 (taken from Ramos Almeida et al. 2011).

Appendix C: Optical data of PKS 1151–34 and companion

Figure C.1 shows the GMOS-S/Gemini optical broad-band image of PKS 1151–34 from Ramos Almeida et al. (2011). The presence of a companion SW of the host galaxy of PKS 1151–34 can be clearly seen. A tail appears to connect the two galaxies. To confirm that the two objects are indeed at similar distance, we use the X-Shooter spectrum published by Santoro et al. (2020) which, interestingly, had the slit aligned with the nucleus of the companion. The spectrum shows clear absorption lines, so the redshift could be measured. From measurements of 4 absorption lines in this Xshooter spectrum the derived redshift is $z_{\rm comp}$ = 0.25702 ± 0.00003. This means that we confirm the galaxy as a companion, blueshifted by –215 ± 25 km s^{-1} in the rest-frame of PKS 1151–34 and blueward of the strongest H I absorption.

Appendix D: Radio continuum images

Figure D.1 shows the radio continuum images of the extended sources. The parameters of the images are given in Table 1.

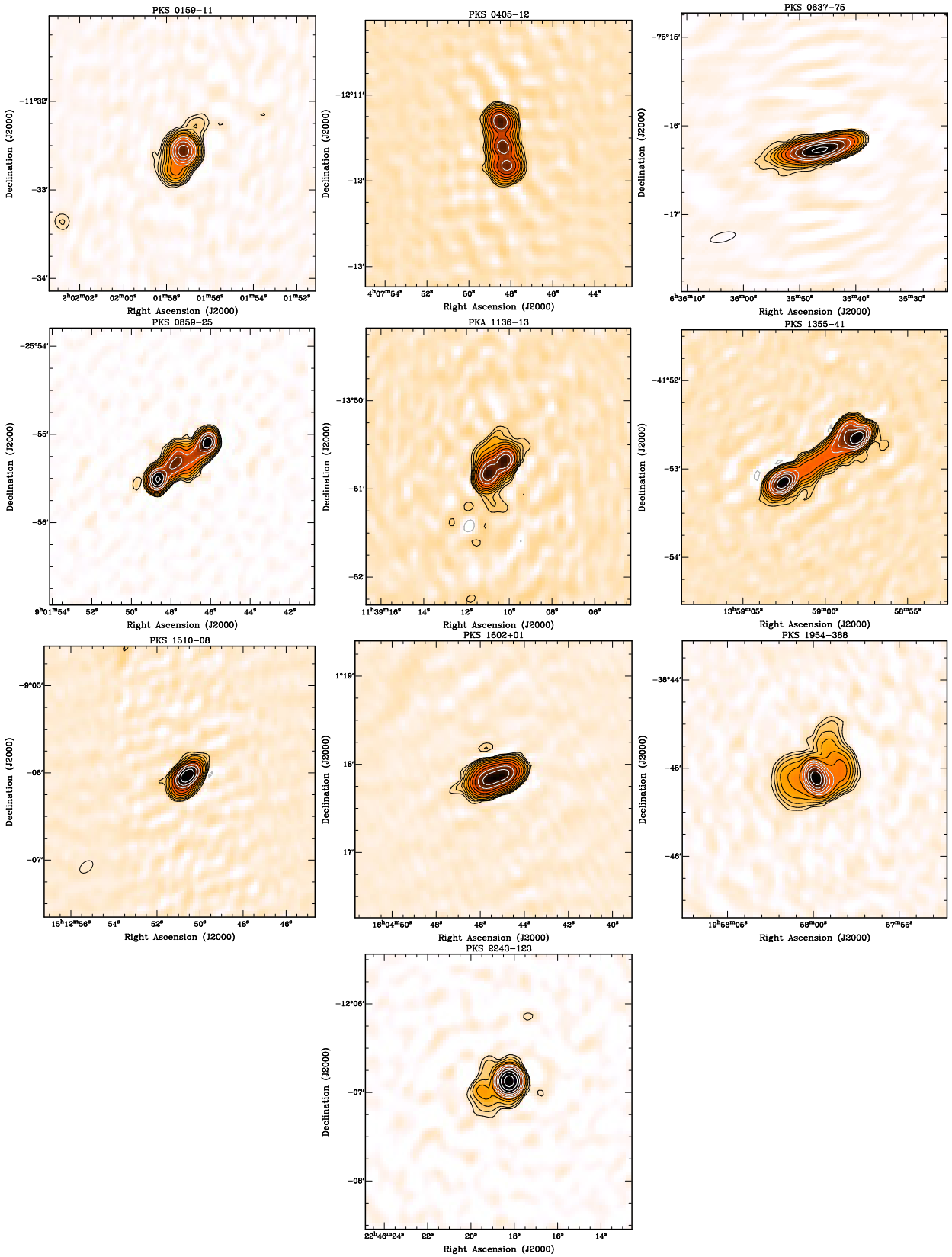

Fig. D.1. Images of the sources with extended radio continuum emission. PKS 0159–11.:Contour levels are 2, 4, 8, ... mJy beam^{-1}; PKS 0405–12: Contour levels are 5, 10, 20 ... mJy beam^{-1}; PKS 0637–75: Contour levels are 5, 10, 20, ... mJy beam^{-1}; PKS 0859–25: Contour levels are 4, 8, 16, 32, ... mJy beam^{-1}; PKS 1136–13: Contour levels 5, 10, 20, 40, ... mJy beam^{-1} ; PKS 1355–41: Contour levels are 2, 4, 8, 16, ... mJy beam^{-1}; PKS 1510–08: Contour levels are 3, 6, 12, ... mJy beam^{-1}; PKS 1602+02: Contour levels are 2, 4, 8, ... mJy beam^{-1}; PKS 1954–388: Contour levels are 0.5, 1, 2, 4, ... mJy beam^{-1}; PKS 2243–1123: Contour levels are 1, 2, 4, ... mJy beam^{-1}..